JACS
JOURNAL OF THE AMERICAN CHEMICAL SOCIETY

Article

pubs.acs.org/JACS

Ru Nanocrystals with Shape-Dependent Surface-Enhanced Raman Spectra and Catalytic Properties: Controlled Synthesis and DFT Calculations

An-Xiang Yin,† Wen-Chi Liu,† Jun Ke, Wei Zhu, Jun Gu, Ya-Wen Zhang,* and Chun-Hua Yan*

Beijing National Laboratory for Molecular Sciences, State Key Laboratory of Rare Earth Materials Chemistry and Applications, PKU-HKU Joint Laboratory in Rare Earth Materials and Bioinorganic Chemistry, College of Chemistry and Molecular Engineering, Peking University, Beijing 100871, China

Supporting Information

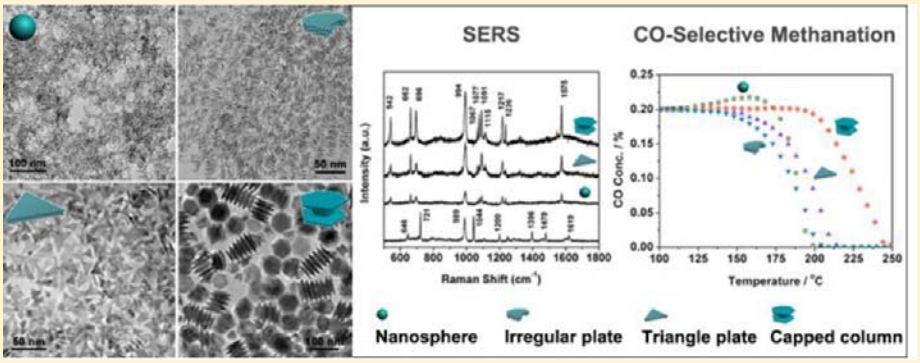

ABSTRACT: Despite its multidisciplinary interests and technological importance, the shape control of Ru nanocrystals still remains a great challenge. In this article, we demonstrated a facile hydrothermal approach toward the controlled synthesis of Ru nanocrystals with the assistance of first-principles calculations. For the first time, Ru triangular and irregular nanoplates as well as capped columns with tunable sizes were prepared with high shape selectivity. In consistency with the experimental observations and density functional theory (DFT) calculations confirmed that both the intrinsic characteristics of Ru crystals and the adsorption of certain reaction species were responsible for the shape control of Ru nanocrystals. Ultrathin Ru nanoplates exposed a large portion of (0001) facets due to the lower surface energy of Ru(0001). The selective adsorption of oxalate species on Ru(10−10) would retard the growth of the side planes of the Ru nanocrystals, while the gradual thermolysis of the oxalate species would eliminate their adsorption effects, leading to the shape evolution of Ru nanocrystals from prisms to capped columns. The surface-enhanced Raman spectra (SERS) signals of these Ru nanocrystals with 4-mercaptopyridine as molecular probes showed an enhancement sequence of capped columns > triangle nanoplates > nanospheres, probably due to the sharp corners and edges in the capped columns and nanoplates as well as the shrunk interparticle distance in their assemblies. CO-selective methanation tests on these Ru nanocrystals indicated that the nanoplates and nanospheres had comparable activities, but the former has much better CO selectivity than the latter.

INTRODUCTION

Morphology-controlled synthesis of metal nanocrystals endows them with important applications in catalysis,[1] imaging,[2] sensing,[3] photonics,[4] and so forth. With different shapes and structures, noble metal nanocrystals would give distinct physical and chemical properties. The adsorption energy of adsorbates and the activation energy of reactions vary on different metal facets since their surface atomic and electronic structures are different.[5] As a result, activity and selectivity for many heterogeneous reactions and electrocatalytic reactions can be tuned and optimized by tailoring the size, morphology, and exposing facets of metal nanocatalysts.[1c,5] Metal nanocrystals with different size, shapes, and aspect ratios exhibit distinct localized surface plasmonic resonance (LSPR) and surface-enhanced Raman spectra (SERS) properties.[6] For instance, Au nanorods showed red-shifted LSPR spectra with increased aspect ratios,[7] and the coating of Au nanorods with Ag shells would shift their LSPR peaks to shorter wavelengths.[8] Starfish-like Rh nanocrystals showed enhanced SERS signals compared to spherical ones.[9] In short, controlled synthesis of noble metal nanocrystals gives us opportunities to tailor their properties and applications. Delicate control over the crystallization and growth process is in the center of the artificial synthesis of nanostructured materials with designed sizes, morphologies, and structures. General parameters for guiding the crystallization of nanocrystals can be classified into two categories: the intrinsic properties of inorganic nanocrystals and the

Received: September 19, 2012
Published: November 26, 2012

dx.doi.org/10.1021/ja3090934 | J. Am. Chem. Soc. 2012, 134, 20479−20489

surrounding growing environments: (1) The symmetry of metal nanocrystals would be determined by the atomic lattice structure of certain metals. The morphology and the exposing facets of a certain naocrystal would be determined by the minimization of its total energy (bulk energy and surface energy). (2) The surrounding environment can alter the thermodynamic and kinetic parameters for the crystallization and growth of nanocrystals.[6] With the assistance of facet-selective adsorption agents, stable nanocrystals with different exposing facets could be prepared with ease.[6]

Ru-based nanocrystals are proved to be of great significance in several heterogeneous and electrocatalytic reactions.[1c,5,10] For instance, Ru catalysts are widely employed in reactions including the synthesis of ammonia,[1c,5] hydrogenation,[1c,5] Fischer−Tropsch synthesis,[1c,5] CO oxidation,[10a] CO methanation,[10b−d] and CO_2 methanation,[10e] etc. The activity and selectivity of Ru-based catalysts for these structure-sensitive reactions would be strongly dependent on the morphology and surface structures of Ru nanocrystals. Therefore, the morphology- and size-controlled synthesis of Ru nanocrystals would build a solid foundation for tuning and optimizing their catalytic performances in these important reactions. However, up to date, the synthesis of Ru nanocrystals still remains a grand challenge.[6b] Ru nanocrystals prepared from both polyol and aqueous solutions do not have well-defined shapes as compared with the finely controlled synthesis of fcc-structured noble metal nanocrystals (Ag, Au, Pd, Pt, Rh, and their alloys, binary structures, etc.).[6b,10a,11] The relatively low ox/red potentials, along with the hcp structures and different surface adsorption properties of Ru crystals, would raise the difficulty in the morphology-controlled preparation of Ru nanocrystals. Therefore, proper kinds of reductants and facet-selective adsorption agents should be selected to realize the controlled synthesis of Ru nanocrystals with well-defined morphologies.

Here, we report the controlled synthesis of Ru nanocrystals with different morphologies and sizes, including ultrathin Ru triangle nanoplates, irregular plates, Ru-capped columns with tunable column lengths, and Ru spherical nanocrystals, through a facile hydrothermal approach in aqueous solutions that we developed in our previous works on the controlled synthesis of Pt-based nanocrystals.[12] The intrinsic structure characteristics, adsorption effects of certain facet-selective agents, and the perturbations of the surrounding environment during the growing process were proved to be critical for the morphology control of Ru nanocrystals. These differently shaped Ru nanocrystals were found to exhibit shape-dependent SERS and catalytic properties, indicating a robust strategy to tailor and optimize functional nanomaterials by designed and controlled chemical synthesis.

EXPERIMENTAL SECTION

The synthesis was carried out using a hydrothermal process with commercially available reagents. $RuCl_3{\cdot}xH_2O$ (A.R., Shengyang Institute of Nonferrous Metal, China), $Na_2C_2O_4$ (A.R., Beijing Chemical Works, China), $Na_2C_3H_2O_4{\cdot}H_2O$ (C.P., Sinopharm Chemical Reagent Co. Ltd.), poly(vinylpyrrolidone) (PVP; $M_w \sim$ 29 000, Sigma-Aldrich), HCHO solution (40 wt %; A.R. Beijing Yili Fine Chemical Reagent Corp., China), and acetone (A.R.) were used as received. The water used in all experiments was ultrapure (Millipore, 18.2 MΩ).

Synthesis of Ultrathin Ru Triangle Nanoplates. In a typical synthesis of Ru triangle nanoplates, 0.06 mmol of $RuCl_3{\cdot}xH_2O$ and 100 mg of PVP were dissolved in 10 mL of water. Then, 0.4 mL of HCHO (40 wt %) was added, and the total volume of the solution was adjusted to 15 mL with water. The homogeneous black solution was transferred to a 25 mL Teflon-lined stainless steel autoclave and sealed. The autoclave was then heated at 160 °C for 4 h before it was cooled to room temperature. The black nanoparticles were centrifuged at 7500 rpm for 10 min with importing 45 mL of acetone and washed with water/acetone three times.

Synthesis of Ultrathin Ru Nanoplates with Irregular Shapes. The synthesis of ultrathin Ru nanoplates with irregular shapes was similar to that of Ru triangle nanoplates except that the amounts of $RuCl_3{\cdot}xH_2O$ and PVP were increased to 0.45 mmol and 200 mg, respectively.

Synthesis of Ru-Capped Columns. In a typical synthesis of Ru-capped columns, 0.12 mmol of $RuCl_3{\cdot}xH_2O$, 80 mg of $Na_2C_2O_4$, and 100 mg of PVP were dissolved in 10 mL of water. Then, 0.4 mL of HCHO (40 wt %) was added, and the total volume of the solution was adjusted to 15 mL with water. The homogeneous black solution was transferred to a 25 mL Teflon-lined stainless steel autoclave and sealed. The autoclave was then heated at 160 °C for 8 h before it was cooled to room temperature. The black nanoparticles were centrifuged at 7500 rpm for 10 min with importing 45 mL of acetone and washed with water/acetone three times.

Synthesis of Ru-Capped Columns with Elongated Trunk. The synthesis of Ru-capped columns with elongated trunk was similar to that of Ru-capped columns except that the hydrothermal treatment temperature was lowered to 150 °C and the reaction time was extended to 24 h or more.

Synthesis of Ru Nanospheres. Ru nanospheres were prepared with a similar method for Ru-capped columns except using 140 mg of $Na_2C_3H_2O_4{\cdot}H_2O$ rather than 80 mg of $Na_2C_2O_4$ as the shape-control agent.

Instrumentation. Samples for transmission electron microscopy (TEM) observations were prepared by drying a drop of diluted colloid dispersion of Ru nanocrystals in water on copper grids coated with amorphous carbon membranes. Particle sizes and shapes were examined by a TEM (JEM2100, JEOL, Japan) operated at 200 kV. High-resolution TEM (HRTEM) was performed on a FEG-TEM (JEM2100F, JEOL, Japan) operated at 200 kV. Samples for scanning electron microscopy (SEM) were prepared by drying a drop of diluted colloid dispersion on silicon wafers. SEM analyses were carried out on a FIB (FEI Strata DB-235) system operated at 30 kV. X-ray diffraction (XRD) patterns were obtained on a D/MAX-2000 diffractometer (Rigaku, Japan) with a slit of 1/2° at a scanning speed of 4° min^{-1} using Cu Kα radiation. Inductively coupled plasma-atomic spectroscopy (ICP-AES) analysis was performed on a Profile Spec ICP-AES spectrometer (Leeman, USA).

First-Principles Calculations. Density functional theory (DFT) calculations were performed with the Vienna Ab initio Simulation Package (VASP) code. The exchange-correlation energy functional is described in the Perdew−Burke−Ernzerhof generalized gradient approximation (GGA). The atoms are simulated using projector augmented-wave (PAW) pseudopotentials. The kinetic energy cutoff for the plane-wave basis set is 500 eV. For the Brillouin zone integration, a 3 × 3 × 1 Monkhorst−Pack special k-point mesh is used to calculate the 3 × 3 × 8 supercells (with four fixed layers and 10 Å of vacuum).

SERS Properties. The SERS spectra were recorded using a Jobin−Yvon HR800 Laser Raman Microscope with lasers of different wavelengths (325, 488, and 633 nm). The substrates for SERS were prepared by drying 1 mL of aqueous dispersion of the as-prepared Ru nanocrystals on silicon wafers. The samples were then incubated in an aqueous solution of 4-mercaptopyridine (10 mM) for 1 h, rinsed with water, and dried in air.

CO-Selective Methanation Reaction Studies. The catalytic activities of the Ru nanoplates, capped columns, and nanoparticles for CO-selective methanation in H_2 and CO_2 streams were measured using a homemade reactor connected with a gas chromatograph. The Ru nanocrystals, which had been washed several times to remove the excess PVP, were loaded onto commercial TiO_2 support (Alfa Aesar) such that each catalyst contained 1.0 wt % Ru (determined by ICP-AES). The catalysts were initially screened using a gas feed composed

of 0.2% CO (99.999%), 20% CO_2 (99.995%), 60% H_2 (99.999%), and balance He (99.999%). In each test, 1 g of the Ru/TiO_2 catalysts was placed in a quartz tube of the homemade fixed bed reactor with the gas speed of 40 SCCM. An online gas chromatograph (Agilent 7890A, USA) with a carbon molecular sieve column (Carboxen 1000, Supelco, USA), a thermal conductivity detector (TCD), and a flame ionization detector (FID) was used to analyze the outlet gas compositions.

RESULTS AND DISCUSSION

Synthesis and Characterization of Ultrathin Ru Nanoplates. Ultrathin Ru nanoplates can be prepared through the method presented in the Experimental Section. With the reduction of $RuCl_3 \cdot xH_2O$ precursors by formaldehyde (HCHO) in a hydrothermal process, triangular or irregular Ru nanoplates could be obtained with high shape selectivities and narrow size distributions.

Herein, detailed characterizations of the as-prepared ultrathin Ru nanoplates were shown in Figures 1−3. As shown in Figure

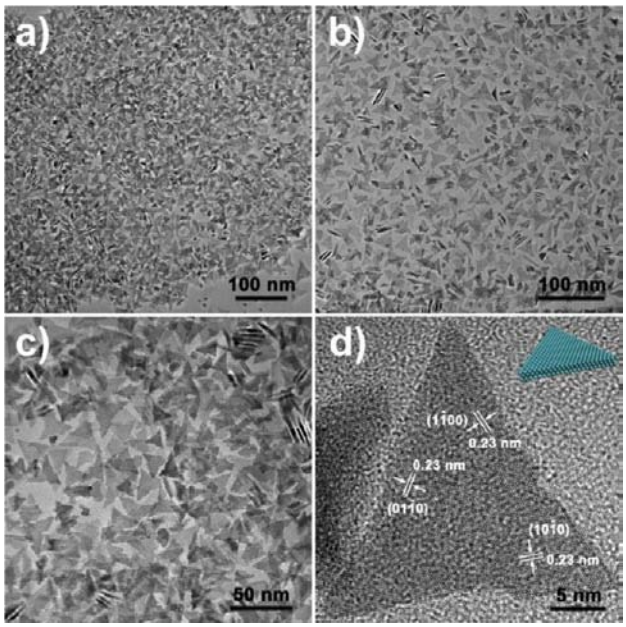

Figure 1. TEM (a−c) and HRTEM (d) images of triangle Ru nanoplates (inset in panel d is the geometric model of the nanoplates).

1, triangle nanoplates with the edge length of (23.8 ± 4.6) nm could be obtained with relatively low precursor concentrations. HRTEM images (Figure 1d) revealed that the side planes of these triangle nanoplates were Ru(1−100), Ru(10−10), and Ru(01−10) facets, and the basal planes were Ru(0001) facets. The corresponding interplane distance measured was 0.23 nm, which was well in accordance with the standard value (2.33 Å) for the {10−10} planes of hcp Ru ($P6_3/mmc$) crystals (JCPDS 06-0663). TEM and HRTEM images in Figures 1d, 3a, and Figure S1 in the Supporting Information (SI) indicated the existence of a high level of defects (e.g., stacking faults) in the structures of the triangle nanoplates. The forming of defects in the triangle nanoplates could be ascribed to the possible fast layered growing rate of Ru nanocrystals under hydrothermal treatments. With increased concentrations of Ru precursors and enhanced reducing rates, smaller Ru nanoplates (with the edge length of (15.1 ± 2.7) nm) with irregular planar shapes could be obtained (Figure 2). The reasons for the formation of these irregular shapes (multipod-like shapes) of these nanoplates

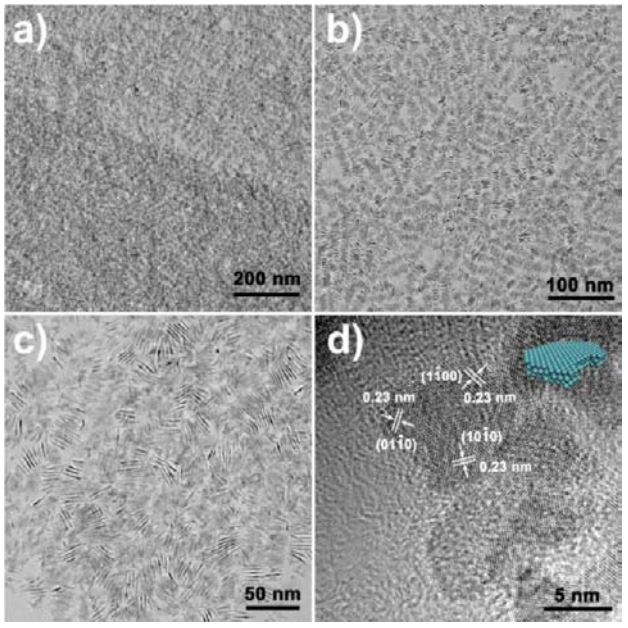

Figure 2. TEM (a−c) and HRTEM (d) images of ultrathin Ru nanoplates with irregular planer shapes (inset in panel d is the geometric model of the nanoplates).

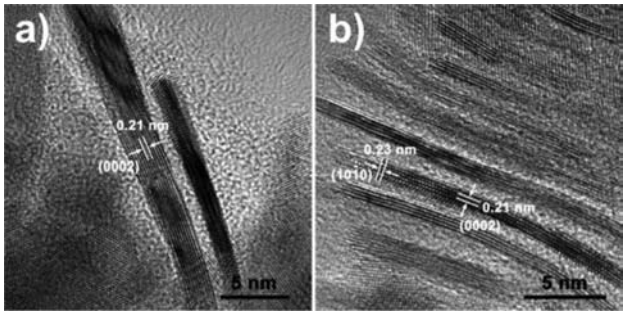

Figure 3. HRTEM images of Ru nanoplates projected perpendicular to the *c* axis: (a) triangle plates and (b) irregular plates.

could be ascribed to the even faster growing rate at higher precursor concentrations.[6,13] Interestingly, due to the flexibility of ultrathin plates, these Ru nanoplates would bend and assemble into layered structures in a face-to-face manner on the carbon membranes of the copper grid (Figure 3b).

HRTEM images of the vertical Ru nanoplates (which were perpendicular to the carbon membrane and thus to the object plane of the TEM) revealed that the axis of both the triangle and irregular plates was along the *c* axis of hcp Ru crystals, and the distance between neighboring planes was measured to be 0.21 nm, which matched well with the distances between (0002) planes of Ru crystals (2.13 Å, JCPDS 06-0663). The thickness of triangle nanoplates was less than 4 nm (3.0 ± 0.6 nm). The irregular nanoplates were less than 2 nm (1.5 ± 0.2 nm) in thickness, containing less than five layers of Ru unit cells in them.

The XRD patterns of the obtained Ru nanocrystals were shown in Figure S2 in SI. The broadened (002) and (101) peaks together with the hardly detected (102) peak in the XRD pattern of the irregular nanoplates indicated that a preferred orientation was adopted by the nanoplates. The basal planes of the nanoplates were Ru (001) facets, and the nanoplates were ultrathin, as confirmed by the TEM and HRTEM measure-

dx.doi.org/10.1021/ja3090934 | J. Am. Chem. Soc. 2012, 134, 20479−20489

ments. Interestingly, the diffraction peaks for the triangle nanoplates deviated from the standard data, indicating the existence of crystalline defects in these triangle nanoplates. Conventionally, the hcp lattice is described by the stacking sequence of *ABAB*... along the [0001] axis. However, due to the existence of stacking faults (Figure 3a, Figure S1 in SI) generated during the growth of the triangle nanoplates, the crystal lattice might adopt the stacking sequence of *AB(C)-ABAB*....[14] As a result, the XRD pattern of the triangle nanoplates would show diffraction peaks corresponding to both of the stacking sequences (Figure S2 in SI).

Synthesis and Characterization of Ru-Capped Columns. Ru-capped columns could be obtained when a certain amount of sodium oxalates ($Na_2C_2O_4$) were introduced into the synthesis (c(Ru):c($Na_2C_2O_4$) = 1:5). As shown in Figure 4,

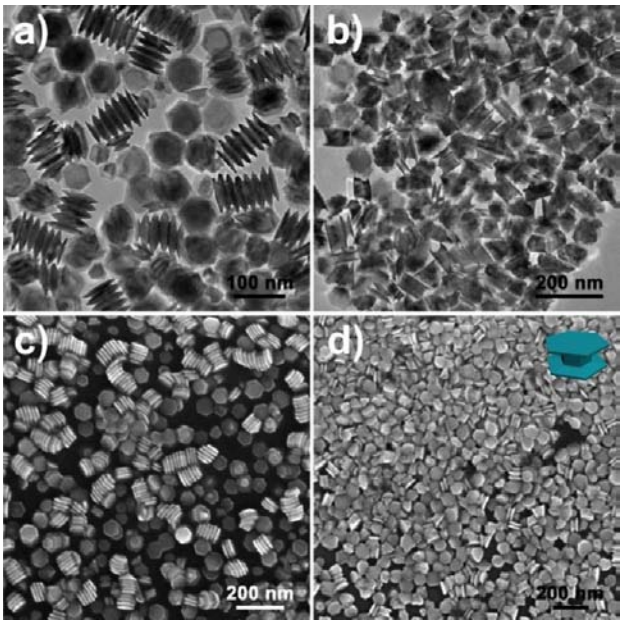

Figure 4. TEM (a,b) and SEM (c,d) images of Ru-capped columns prepared under 160 °C (a,c) and 150 °C (b,d) (inset in panel d is the geometric model of the capped columns).

these capped-column-like nanocrystals could be divided into two parts: the columns at the center of the nanocrystals and the hexagonal plates at both ends of the nanocrystals. The trunk lengths of these capped columns could be tuned by changing the reaction temperature and time. As shown in Figure 4b,d, the trunk could be elongated by lowering the reaction temperature to 150 °C.

HRTEM images of the capped columns confirmed that they were single-crystalline Ru nanocrystals with the lattice constants in consistency with the standard data of hcp Ru crystals (JCPDS 06-0663). The axial direction of both the columns and plates was along the c axis, and the terminal plane of the end plates was the basal (0001) facet of hcp Ru nanocrystals. The FFT (Fast Fourier Transfer) pattern (Figure 5a, inset) of the HRTEM image and enlarged HRTEM images (Figure S3 in SI) confirmed that the two plates and the trunk shared the same crystal lattice and that the whole capped column nanocrystal was single crystalline. These capped columns always showed a sharp transition between the trunk and the two terminal plates at both ends (Figure 5b and Figure S4 in SI), indicating that a unique morphology evolution

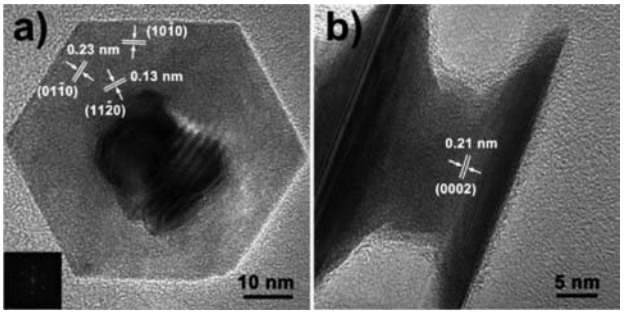

Figure 5. HRTEM (a,b) images of Ru-capped columns prepared under 160 °C, (a) along and (b) perpendicular to the ⟨0001⟩ direction. Inset in panel a is the FFT pattern of the whole HRTEM image.

process would be adopted by these Ru-capped-column-like nanocrystals during the synthesis procedure. The XRD pattern (Figure S2 in SI) of the obtained Ru-capped columns was in good accordance with the standard one of hexagonal Ru crystals (JCPDS 06-0663). In addition, as shown in Figure 5b, terminal planes of capped columns prepared at 160 °C were very flat, and these capped columns would thus self-assemble into a string with a face-to-face manner in short distances and into large dendrites in long distances (Figures 4a,c, 5b, and Figures S4 and S5 in SI).

Interestingly, besides those capped columns whose ending plates were of similar sizes, those with two ending plates of significantly different sizes could also be observed in the as-prepared capped-column-like nanocrystals (Figure 4c and Figure 6). As shown in Figure 6, a large plate was connected to a much smaller one through a short axle. The proposed growing mechanism for these asymmetrical capped columns will be discussed below in detail.

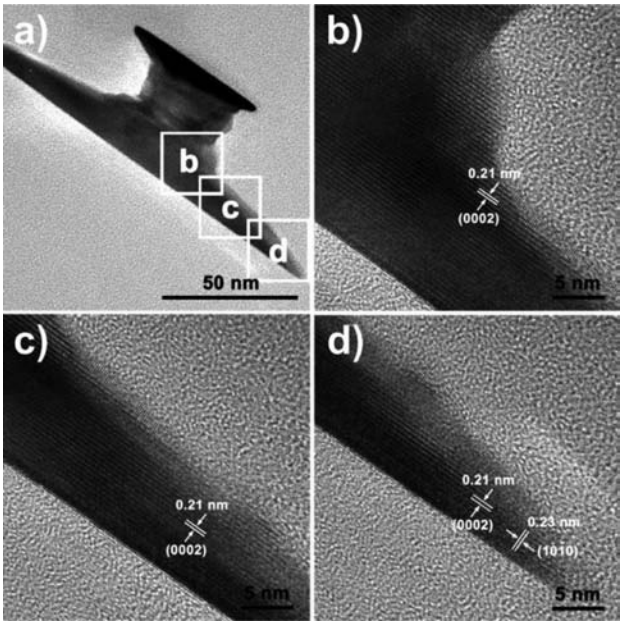

Figure 6. HRTEM images of Ru-capped column nanocrystals with two differently sized plates at the ends of a column. The projection axis was perpendicular to the c direction of Ru nanocrystals. Panels b–d are enlarged HRTEM images for the corresponding parts of the capped column in panel a, respectively.

dx.doi.org/10.1021/ja3090934 | *J. Am. Chem. Soc.* 2012, 134, 20479–20489

Notably, the final morphologies of Ru nanocrystals were very sensitive to the molar ratios of the Ru(III) precursor to sodium oxalate. As shown in Figures S6 and S7 in the SI, no Ru-capped columns could be obtained with Ru/oxalate ratios deviating far from 1:5 in the synthesis, and no Ru-capped columns could be observed at a lower concentration of Ru precursors and oxalates with their molar ratio fixed at 1:5. These results emphasized that the combined actions of coordination strength between Ru(III) ions and oxalate and ligands, the decomposition rates of oxalate species, and the reduction/nucleation rates of Ru were critical to the formation of Ru-capped columns.

Growth Mechanism for Ru Nanocrystals with Different Morphologies. The size and shape evolution process of noble metal nanocrystals would be influenced by several parameters, including their intrinsic properties and the external regulations over their nucleation and growth steps.

The size and size-distribution control of Ru nanocrystals was similar to those of other noble metal nanocrystals and followed the LaMer model and the size-distribution focusing and defocusing principle.[6,13] The high reaction temperatures and rapid heating rates ensured the relatively rapid nucleation rates and narrow size distributions of Ru nanocrystals. In the synthesis of triangle or irregular nanoplates, with the use of a higher concentration of Ru(III) precursor, more nuclei would be generated quickly at the nucleation stage, and thus nanoplates with shorter edge lengths and thinner thickness could be obtained (Figures 1−3). In the synthesis of Ru-capped columns, Ru(III) species were mostly in the form of $[Ru(III)(ox)_3]^{3-}$ before being reduced by HCHO, as confirmed by the extinction spectra and the color of the reaction solutions (Figure 7 and Figure S8 in SI). The adsorption peaks at 285 and 353 nm (shoulder peak) confirmed that Ru(III) oxalates ($[Ru(III)(ox)_3]^{3-}$) were generated in the first hour of the hydrothermal treatment.[15]

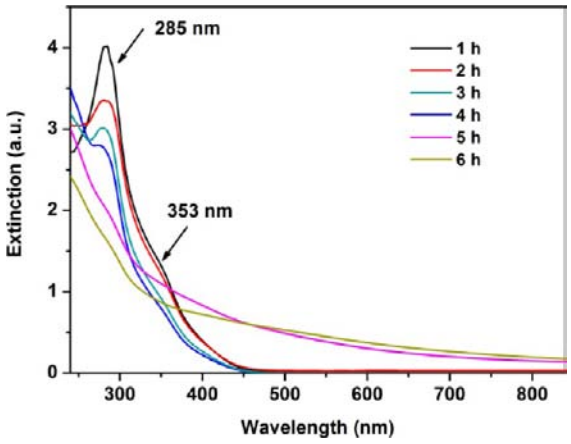

Figure 7. Time-sequential extinction spectra of the solutions or dispersions (Figure S8 in SI) obtained from the synthetic reaction of Ru-capped column nanocrystals.

Therefore, in this case the nucleation was achieved by the following reducing reactions

$$[Ru(III)(ox)_3]^{3-} + HCHO \rightarrow [Ru(II)(ox)_3]^{4-} + CO_x + H^+$$

$$[Ru(II)(ox)_3]^{4-} + HCHO \rightarrow Ru(0) + ox^{2-} + CO_x + H^+$$

Compared to the standard red/ox potentials of Ru^{3+}/Ru^{2+} and Ru^{2+}/Ru (0.25 and 0.46 eV, respectively),[16a] the red/ox potentials of $[Ru(III)(ox)_3]^{3-}/[Ru(II)(ox)_3]^{4-}$ would drop to a much lower and negative value,[16b] resulting in the much slower reducing rate of the Ru species. Thus, according to the nucleation principles,[6,13] the strong coordination effect of oxalates on Ru(III) ions would lead to the reducing of nuclei numbers and the formation of nanocrystals with much larger sizes in the preparation of capped column nanocrystals.

The morphology evolution mechanism for Ru nanocrystals would be more complicated. On one hand, the nanocrystals produced during the hydrothermal process would attempt to minimize their total surface free energy with a given volume and thus tend to expose their most stable facets.[6] On the other hand, the final morphologies of Ru nanocrystals could be regulated through the fine control over the facet-selective adsorption effects of certain capping agents. Moreover, the simultaneous variation of the reaction environment (e.g., precursor concentration, adsorption strength, etc.) during the growing process of nanocrystals would also exert significant effects on the shape evolutions of noble metal nanocrystals. The hcp structure of Ru crystals endows them with the possibility to grow into more anisotropic morphologies, e.g., hexagonal plates, triangle plates, hexagonal prisms, etc., similar to the observation in the synthesis of hcp Co nanocrystals.[17] And the variation of surrounding environments would add even more possibilities to the shape evolution of Ru nanocrystals.

DFT calculations, as proved to be a helpful tool for comprehending the facet-selective adsorption mechanism of citrates on different facets of Ag nanocrystals,[18] were carried out to help elucidate the growing mechanism for Ru nanocrystals and to clarify the effects of the intrinsic properties of Ru crystals and external surrounding environments on the shape evolution of Ru nanocrystals. Both the surface energy and the adsorption energy of different reaction intermediates on Ru(0001) (basal facets) and Ru(10−10) (prism facets) were calculated through the method described in the Experimental Section. Two kinds of Ru(10−10) surfaces (denoted as $(10-10)_a$ and $(10-10)_b$) were cleaved. As shown in Figure 8a, the surface energy of Ru(0001) was 1.06 eV/surface atom (2.65 J/m^2), while the surface energy was 2.64 or 2.18 eV/surface atom (3.61 or 2.98 J/m^2) for $Ru(10-10)_a$ or $Ru(10-10)_b$, respectively. The surface energy of Ru(0001) was 0.96 or 0.33 J/m^2 lower than that of $Ru(10-10)_a$ or $Ru(10-10)_b$, respectively. These calculation results were in good consistency with previous results suggested by Skriver and co-workers (0.93 or 0.30 J/m^2 lower for Ru(0001) than $Ru(10-10)_a$ or $Ru(10-10)_b$, respectively).[19] The much lower surface energy of Ru(0001) than those of Ru(10−10) suggested that the intrinsic growth of Ru nanocrystals under thermodynamic control would attempt to expose the most stable (0001) facets to minimize their total surface free energy. Therefore, these Ru nanocrystals would adopt the radial growth manner (growth in the *ab* plane of hcp crystal) and grow into two-dimensional (2D) nanoplates with the absence of any further morphology regulations.

This prediction was well in accordance with our experimental observations. PVP was reported to show no significant facet-selective adsorption effects on small nanocrystals.[6] In our synthesis of ultrathin nanoplates, the change of the amounts or

dx.doi.org/10.1021/ja3090934 | J. Am. Chem. Soc. 2012, 134, 20479−20489

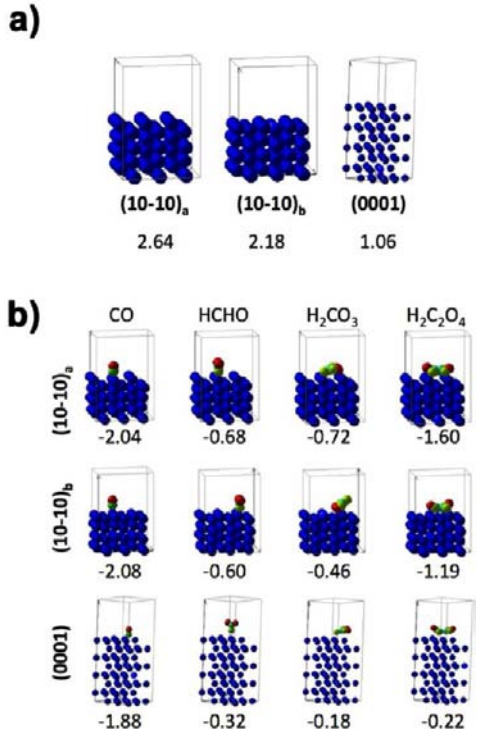

Figure 8. (a) Surface energies (eV/surface atom) of $Ru(10-10)_a$, $Ru(10-10)_b$, and Ru(0001) and (b) adsorption energies (eV) of some reaction species on these three surfaces.

the molecular weights of PVP did not make any obvious difference in the shape contours and shape selectivity of Ru nanoplates (Figure S9 in SI), suggesting the poor shape-selective capability for PVP in the synthesis of Ru nanoplates. To evaluate the effects of other possible intermediates generated during the synthesis procedure, the adsorption energies of these intermediates and the top view of the adsorption geometries of oxalate species on Ru surfaces were calculated and shown in Figure 8 and Table S1 and Figure S10 in SI. Formaldehyde, as well as the possible intermediate CO and the final product CO_2 (in the form of H_2CO_3 under hydrothermal treatment), showed stronger adsorption on Ru(10−10) than that on Ru(0001). However, considering the low concentration of reaction intermediates (e.g., CO), the instability of H_2CO_3, and the much lower surface energy of Ru(0001) (1.58 or 1.12 eV/surface atom lower as compared with $Ru(10-10)_a$ or $Ru(10-10)_b$), the differences in the adsorption of HCHO, CO, and H_2CO_3 on different Ru surfaces would not be large enough to inhibit or retard the radial growth of Ru nanocrystals. As a result, to expose large portions of the (0001) facet with much lower surface energies, the Ru nanocrystals would then grow into the shape of ultrathin nanoplates.

On the contrary, the calculated adsorption energy of oxalates on Ru(10−10) (−1.60 or −1.19 eV for $Ru(10-10)_a$ or $Ru(10-10)_b$) are much larger than that on Ru(0001) surfaces (−0.22 eV). The significant differences in adsorption energies of oxalates on different Ru surfaces ((10−10) vs (0001)) could be briefly ascribed to the structure symmetry match between the oxalate molecules and the Ru atoms on certain surfaces. The oxalate dianion, with a D_{2h} molecular symmetry, would match well with the symmetry of Ru(10−10) and have all of the four oxygen atoms adsorbed on different surface Ru atoms. However, on Ru(0001), the hexagonal symmetry of surface Ru atoms would not match the D_{2h} molecular symmetry of oxalate dianions, and therefore the adsorption energy would be much lower. These results indicated that oxalate species would selectively adsorb on the prism planes of Ru-capped columns and retard the growth on their prism planes. Thus, the preferential growth direction of Ru nanocrystals would be along the axial direction due to the facet-selective adsorption and constraining effects of oxalates on the prism plane of Ru nanocrystals. Ideally, Ru nanoprisms or nanowires with large prism planes could be expected as the final products with constant or proper adsorption strength of oxalates on their prism planes.

However, the experiment results were different. No perfect hexagonal prisms but capped-column-like nanocrystals were obtained with the use of a certain amount of oxalates as facet-selective adsorption agents, and the shape evolution of these capped columns should follow a unique growing mode that can be divided into two steps: (a) the axial growth of the trunk and (b) the radial growth of the end plates. As shown in Scheme 1,

Scheme 1. Proposed Growing Model of Ru-Capped Columns

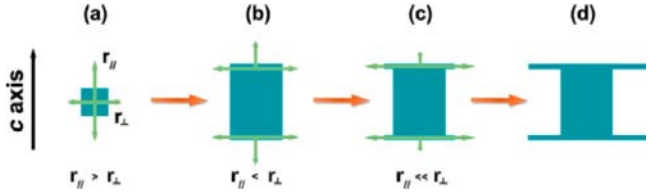

in the first step, the axial growth of Ru nanocrystals ($r_{\parallel} > r_{\perp}$), as confined and directed by the selective adsorption of oxalate species, would lead to the formation of the trunk (Scheme 1a). In the second step, the preferred growth direction changed into the radial direction ($r_{\parallel} < r_{\perp}$) and large plates would grow out at both ends of the trunk (Scheme 1b−d). The cause responsible for the alternation of the growing modes from the axial one to the radial one should come from the perturbation of the reaction solutions during the present hydrothermal processing.

Lessons come from nature. Capped-column-like snowflakes (ice crystals, hcp structure) can be observed both in nature and in laboratories.[20] Direct observations and calculation simulations by Libbrencht et al. and other researchers suggested that the formation of capped-column-like ice crystals was also guided by a two-stage growing mechanism.[20,21] In the first stage, ice crystals grow into hexagonal prisms due to their faster growing rate along the *c* axis. Then, due to the perturbation of the surrounding environments (e.g., temperature, supersaturation of water steam, etc.), the growth of ice crystals turns into the second stage in which radial growth is preferred. Thin hexagonal plates would be formed at one or two end(s) of the hexagonal prisms, leading to the formation of capped-column crystals. The perturbations from the environment have played the key role in the transition of these two growing modes and the shape evolution procedure of snowflakes.

A similar growing mechanism was suggested in the present synthesis of the Ru-capped-column nanocrystals. Time-sequential observations (Figure 7 and Figure S8 in SI) revealed that the generation of Ru-capped columns would follow the thermal decomposition of Ru oxalates in solutions. As revealed by the absorption spectra, Ru(III) oxalates ($[Ru(III)(ox)_3]^{3-}$) were generated in the first hour of the hydrothermal

dx.doi.org/10.1021/ja3090934 | J. Am. Chem. Soc. 2012, 134, 20479−20489

treatment.[15] Then, in the following 4 h, the thermally unstable ruthenium oxalates would be decomposed under the vigorous hydrothermal treatment, as indicated by the gradual decrease of the peak intensities of the extinction spectra (Figure 7). The forming of Ru oxalates would significantly delay the reduction of Ru species and the nucleation of Ru nanocrystals. A large amount of Ru nanocrystals were generated at the fifth hour of the hydrothermal treatment, resulting in the significant changes both in the extinction spectra (Figure 7) and in the color of the reaction solutions (Figure S8 in SI). The change of the color from greenish yellow to black indicated the sudden nucleation and following growing stage of Ru nanocrystals due to the decomposition of ruthenium oxalates and the reduction of Ru(III) species by HCHO during the hydrothermal treatment.

Sodium oxalates are stable under hydrothermal treatment in neutral aqueous solutions. However, the oxidation of HCHO by Ru(III) species would increase the concentration of H^+ cations in reaction solutions and thus accelerate the decomposition of oxalic acid during the synthesis process (Figure S11 in SI). The decrease in the concentration of oxalates in solutions would then weaken the selective adsorption and growth-retarding effects of oxalates on the side planes of Ru nanoprisms. At a "critical" point, when the capping effects over Ru nanocrystal side planes were so weak that the radial growing rate ($r_\perp$) would be faster than the axial growing rate ($r_\parallel$), thin plates would grow out at one or two ends of the trunk, leading to the formation of columns with thin plates (Scheme 1c). Once these thin caps were formed, the so-called thin edge instability would amplify the small changes in crystal growth and thus accelerate the growth of thin plates, leading to the formation of capped columns with large plates at the end(s) of the trunk (Scheme 1d).[20,21] The perturbation (the decomposition of oxalates) and the edge instability effect, as similar to those observed in the growing of snowflakes,[21] led to the formation of Ru-capped column nanocrystals.

In addition, the starting molar ratio between Ru(III) precursors and oxalates should be critical for the shape control of the Ru-capped columns. On the one hand, the prism-facet-selective adsorption would be not strong enough to restrain the radial growth of Ru nanocrystals with insufficient amounts of oxalates. One the other hand, the coordination and surface-adsorption effects would be too strong to obtain Ru-capped columns with well-defined morphologies. As shown in Figure S6 in the SI, when the oxalate/Ru(III) ratio was kept at 3:1, no capped columns but only large-sphere-like aggregations of small Ru platelets could be observed. When the oxalate/Ru(III) ratio was 4:1, capped columns could be obtained, but with wide size distributions. When the oxalate/Ru(III) ratio was raised to 6:1 or 7:1, only stacks of columns with thick edges and rough surfaces could be prepared due to the too strong coordination and adsorption effect of excess oxalate species.

The effect of PVP molecules on the morphologies of Ru-capped columns was also investigated by varying both their amounts and molecular weights for the synthesis (Figure S12 in SI). In either case, Ru-capped columns could be obtained, indicating that PVP molecules would not show a very significant effect on the shape selectivity of Ru-capped columns.

The length of the trunk of the nanocrysals could be tuned by altering the relative reaction rates for the oxalate decomposition and the ruthenium reduction. At 150 °C, the decomposition of oxalates was much slower (oxalic acid began to decompose quickly at temperatures above 150 °C);[22] the "critical" point for the transition of the growing modes into radial growth would be delayed; and the Ru nanocrystal would stay in the axial growing mode for a relatively long time. As a result, capped columns with an elongated trunk could be obtained. At 160 °C, the thermolysis of oxalates would be faster, and an earlier change from the axial growth to the radial growth would produce capped columns with shorter center columns. The thickness of the plates at the end of the columns would gradually decrease along the radical direction, indicating a self-sharpening behavior caused by the edge instability effects during the growth of thin nanoplates.[21]

Figure S13 in the SI shows the snapshot of the "intermediate" stage of the shape evolution process of the capped columns. Barely capped column-like nanostructures formed under 150 °C at 12 h, which would further grow into capped columns with larger terminal plates (Figure 4b,d), serving as evidence for the rationality of the proposed growth mechanism of the Ru-capped columns. At 160 °C, due to the much faster decomposition of the oxalates and higher reaction temperature, the nucleation and growth of Ru-capped columns were much quicker. Once the nucleation occurred, the nuclei would soon grow and develop into capped columns, making it very difficult to capture the transition state during the shape evolution of the capped columns in the hydrothermal process.

Similar to the observation in snowflakes,[20,21] asymmetrical capped columns (or plates-on-pedestals) could be obtained occasionally (Figure 6). The possible cause for the formation of these capped columns with differently sized plates could be ascribed to the shielding effect of the larger plate upon the smaller one. The two plates were so close together that the one that grew out faster at the beginning would shield the other from the diffusion of Ru precursors in solutions and thus inhibit the growth of the smaller one. As a result, capped columns with two differently sized plates formed. A similar shielding effect was observed and reported by Libbrecht et al. in the growing of snowflakes.[21]

On the basis of the experimental and theoretical evidence discussed above, we suggested a simplified synthesis diagram for the preparation of Ru nanoplates and capped columns, as shown in Scheme 2. Without the addition of sodium oxalates as facet-selective adsorption and shape-directing agents, the Ru nanocrystals would adopt a radial growth (planner growth) mode to form ultrathin triangle nanoplates or irregular nanoplates with different nucleation and growth rates. With higher concentration of Ru precursors, thinner nanoplates with irregular shapes could be obtained due to the relatively faster

Scheme 2. Schematic Synthesis Diagram for Ru Nanoplates and Capped Columns

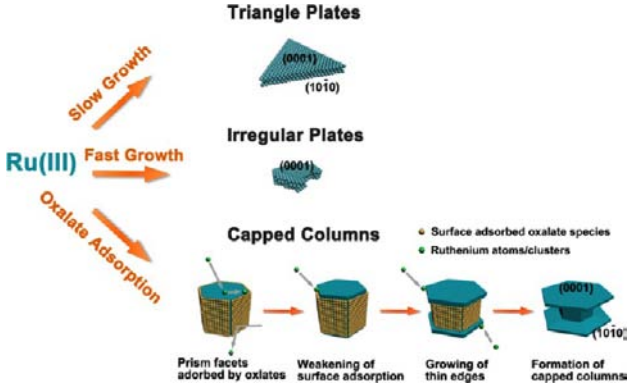

dx.doi.org/10.1021/ja3090934 | J. Am. Chem. Soc. 2012, 134, 20479−20489

nucleation and growth rate as compared with the preparation of triangle nanoplates. Ru-capped columns could be obtained with high selectivity and uniformity with the addition of oxalates, which would selectively adsorb on the prism facets of Ru nanocrystals. At the early state of the synthesis, the concentration of oxalate species in solution would remain at a high level, and the adsorption strength of oxalates on the prism planes of the Ru nanocrystal would be strong enough to retard the growth of Ru nanocrystals perpendicular to the prism facet (the radial growth). Therefore, in this stage of crystallization, growing along the *c*-axis was much preferred, and Ru nanocrystals would grow into the shapes of hexagonal or quasi-hexagonal columns. However, the thermal decomposition of oxalates in acid solutions (with H^+ generated by the oxidation of HCHO by Ru(III) species) would weaken the adsorption effects on prism planes and lead to the growing of thin edges at the ends of columns, where the surface free energy was higher than the central part of the columns. After that, the thin edges at the end(s) of each column would grow into large thin plates due to the reduction and diffusing of more Ru precursors in the solution. The distinct shape evolution process of ultrathin Ru nanoplates and Ru-capped columns demonstrated that the morphology control of Ru nanocrystals could be achieved by both the proper understanding of the intrinsic structure and characteristics of noble metal crystals and the delicate control of the external synthesis environments. These understandings and strategies would further help a lot in studies on shape-dependent properties of Ru nanocrystals.

SERS Property. As is known, Ru usually shows a weak SERS effect, unlike the cases of Au and Ag metals.[23a] It has been demonstrated that shape-controlled metal nanocrystals could exhibit enhanced SERS properties to certain kinds of probe molecules due to their distinct morphologies.[6b,23]

Herein, we compared the SERS activities of Ru thin films consisting of three types of Ru nanocrystals with the morphology of capped columns (Figure 4a,c), triangle nanoplates (Figure 1), and nanospheres (Figures S2 and S14 in SI; 3.0 ± 0.3 nm in diameter), using 4-mercaptopyridine as the probe molecules due to their large Raman scattering cross sections[24] (see Table S2 in SI). Recent studies revealed that nanocrystals with shaper edges or corners would be more active in SERS applications due to the stronger field enhancement near their shape surfaces.[25] Affirmatively, a similar phenomenon was observed in this work with differently shaped Ru nanocrystals used as metal substrates. As shown in Figure 9, it was found that the capped columns and triangle nanoplates gave stronger SERS signals as compared to the spherical Ru nanocrystals mainly due to the sharper edges and corners of these nanostructures in comparison with the nanospheres.

Furthermore, strong electromagnetic field enhancements would arise at the interparticle junctions in nanoparticle aggregates upon interaction with visible radiation.[23b−d] The coupling between the particles was quite short ranged as two particles approach each other within 1 nm.[23b] In this work, Ru nanoplates and capped columns would self-assemble on a substrate. The average interparticle distance for Ru-capped columns in their assemblies was measured to be 0.3 nm (Figure 4a), which was much shorter than that for nanoplates (0.9 nm, Figure 3b). Therefore, there would be stronger electromagnetic field enhancements at the interparticle junctions in the assemblies of Ru-capped columns, which could be the cause for the stronger SERS signal of Ru-capped columns than the nanoplates.

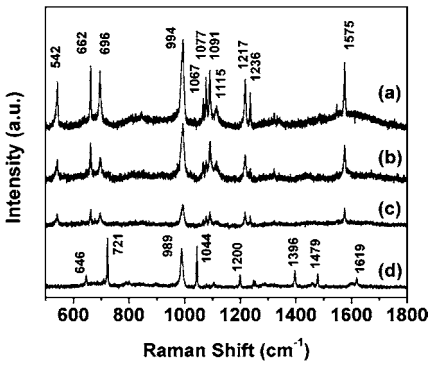

Figure 9. SERS spectra of 4-mercaptopyridine on films of Ru nanocrystals (a−c): (a) capped columns, (b) triangle plates, (c) spherical nanocrystals, and (d) Raman spectra of bulk 4-mercaptopyridine solids.

CO-Selective Methanation Reactivity. To evaluate the shape and size effects of Ru nanocrystals on their catalytic properties, we employed the as-prepared Ru-capped columns (Figure 4a,c), triangle plates (Figure 1), irregular plates (Figure 2), and nanospheres (Figure S14 in SI) in a CO-selective methanation reaction to monitor the variation of the catalytic activity and selectivity on Ru nanocrystals with different morphologies (see Table S2 in SI and Figure S15 in SI).

The CO methanation process is the direct hydrogenation of CO to CH_4 and H_2O with the consumption of three moles of H_2.[10b−d] This process has been studied as a less costly substitute for the preferential oxidation of CO (PROX) to produce "deep-clean" H_2 from syngas for fuel cell or synthesis applications.[10d] The challenges for CO-selective methanation reactions are the side reactions between the coexisting CO_2 in reformate hydrogen fuels and H_2 under high temperatures. The direct hydrogenation of CO_2 (CO_2 methanation), and the reverse water−gas-shift reactions (converting CO_2 and H_2 into CO and H_2O), would result in the large consumption and waste of H_2. As a result, catalyst studies on CO-selective methanation reactions should meet at least two requirements: (1) high activities, diminishing the concentration of CO to several parts per million at proper temperatures and (2) high selectivity, reducing the waste of H_2 caused by side reactions.

Ru-based catalysts have been reported to be the most effective ones for CO-selective methanations.[26] Ru nanoparticles supported by several oxide supports (including TiO_2, Al_2O_3, SiO_2, etc.) were found to show remarkable activity and selectivity in the selective methanation of CO.[10b−d,26] However, due to the lack of delicate controls over the morphologies of Ru nanocrysatals,[6b,11] previous studies are mostly concerned about the catalytic performances of irregular Ru nanoparticles with different sizes, loading amounts, oxide supports, and metal−support interactions.[10b−d,26,27] Herein, on the basis of shape-controlled synthesis of Ru-capped columns, triangle nanoplates, irregular nanoplates, and spherical nanocrystals, we are now able to evaluate the catalytic performance of Ru nanocrystals with different sizes and well-defined morphologies in the CO-selective methanation reactions.

As shown in Figure 10, the CO conversion and CH_4 generation curves show the reaction activity and selectivity of Ru nanocrystals with different morphologies loaded on TiO_2 supports with the same loading amount. Since the CO methanation reaction is insensitive to the surface structure (exposed facets) of the Ru catalysts, as confirmed by Goodman

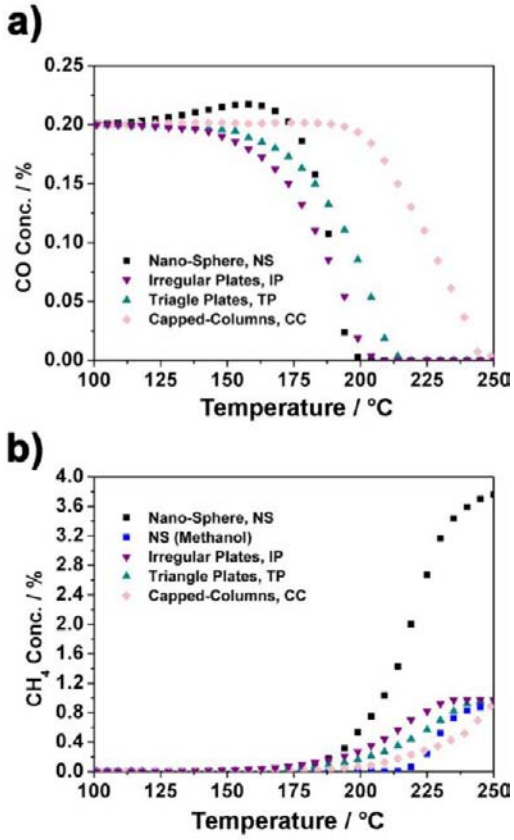

Figure 10. Temperature dependence of (a) CO and (b) CH_4 outlet concentrations over Ru nanocrystals (1 wt % on TiO_2) with the shape of nanosphere (NS), irregular plates (IP), triangle plates (TP), and capped columns (CC) for CO-selective methanation reactions.

and co-workers,[28] the difference in the activity in the present case could be ascribed to the distinct ratio of surface atoms, which served as the active sites in the catalytic reaction. The capped columns, although with sharp edges at the end(s) of each column, showed the lowest reaction activity due to the relatively larger particle sizes and thus lower dispersions of surface Ru atoms. The concentration of the outlet CO remained above 20 ppm until 245 °C and dropped to 7 ppm at 245 °C and 4 ppm at 250 °C. For triangle, irregular nanoplates and spherical nanocrystals, the concentration of residual CO dropped to 3−4 ppm at 214, 204, and 200 °C, respectively, and remained under 10 ppm before the reaction temperature was elevated to above 250 °C. At reaction temperatures higher than 250 °C, the conversion of CO would drop dramatically due to the exothermic nature of the methanation reaction. These results confirmed that, with relatively high surface atom dispersions, ultrathin triangle Ru nanoplates (<4 nm in thickness), irregular nanoplates (<2 nm thick), and spherical nanocrystals (about 3−4 nm in diameter) showed relatively high CO methanation activities in the proper temperature window below 250 °C. As revealed by Figure 10a, the activity sequence for CO methanation reaction of these four kinds of Ru catalysts is: nanospheres > irregular plates > triangle plates ≫ capped columns.

Another requirement for the CO methanation reaction is to enhance the reaction selectivity, which could be conducted from the comparison of the conversion ratio of CO and CH_4 species in the reaction.[29] For nanospheres, the concentration of outlet CH_4 was 0.53% at 200 °C, indicating a selectivity of 38% for the selective methanation of CO against CO_2. This value dropped to about 27% at 204 °C, 14% at 214 °C, and below 5% at 250 °C. For irregular nanoplates, the selectivity of CO was 57%, 35%, and 21% at 204, 214, and 250 °C, respectively. For triangle nanoplates, this value was 56% and 22% at 214 and 250 °C, respectively. These results indicated that in spite of the fact that the spherical nanocrystals showed slightly better activity than nanoplates (irregular and triangle ones) the CO selectivity for nanoplates was significantly higher than that for spherical nanocrystals. Thus, the ultrathin nanoplates (although having a little less activity than spherical nanocrystals) showed significantly higher CO selectivity than spherical nanocrystals while keeping residual CO concentrations below 10 ppm at the temperature range between 204 and 250 °C and could be employed as good candidates for the selective CO methanation reactions.

The low selectivity of CO methanation on Ru nanospheres could be ascribed to be the relatively higher activity to side reactions (reverse water−gas-shift reaction, direct CO_2 methanation, and methanol formation (see Figure 10b)). The CO concentration, initiated at 0.20%, was raised before the temperature of 175 °C and reached a highest value at 0.22% at 160 °C (Figure 10a). The increase of CO concentration could be ascribed to the reverse water−gas-shift process that converted CO_2 into CO and H_2O with the consumption of H_2. In addition, the higher activity for small Ru nanospheres to the side reaction of CO_2 methanation[10e] could also cause the decrease of CO selectivity. As shown in Figure S16 in SI, the concentration of CO_2 (20.0% at the inlet of the reaction) would drop to 15.3% at 250 °C due to the methanation or reverse water−gas-shift reaction on Ru nanospheres, while the values for Ru irregular plates and triangle plates were 18.9% and 19.3%, respectively. The higher CO selectivity (i.e., less active to CO_2 methanation reaction) for nanoplates than that for spherical nanocrystals could be ascribed to the large portions of the Ru(0001) facets as compared to those spherical nanocrystals enclosed by mixed facets.

Further studies on the more detailed catalysis properties and mechanisms for these Ru nanocrystals are still ongoing in our laboratory.

■ CONCLUSIONS

We have demonstrated that Ru nanocrystals with different sizes and morphologies could be obtained through a facile hydrothermal approach with the fine control of reaction parameters. Both experimental results and first-principles calculation revealed that the intrinsic surface energy and the facet-selective adsorption of shape-control agents would play a significant role in the growing and shape evolution process of Ru nanocrystals. The growing of Ru-capped-column-like nanocrystals showed a nature-mimic growth behavior, whose shape-evolution mechanism was similar to the growing of capped-column-like snowflakes. The perturbations of the synthesis environment, i.e., the decomposition of the oxalate species in the reaction solutions, were critical to the formation of Ru nanocrystals with different morphologies. This synthesis strategy could be used to prepare nanocrystals with unusual shapes (e.g., capped columns) and novel properties in future studies. Ru nanocrystals with different morphologies prepared in this work showed distinct SERS properties and catalytic performances. For SERS applications, Ru-capped columns with sharp edges and corners and the rather short interparticle distance (<0.5 nm) in their assemblies exhibited higher signal

enhancements. For CO-selective methanation, Ru nanoplates showed higher catalytic activity and selectivity due to their ultrathin characteristics and the large portions of exposed Ru(0001) facets. This work not only has made significant progress in the shape-controlled preparation of Ru nanocrystals but also shed new light on the understanding of the synthetic mechanism of functional inorganic nanomaterials with unique properties and significant applications.

■ ASSOCIATED CONTENT

Supporting Information

More TEM images and other data are included. This material is available free of charge via the Internet at http://pubs.acs.org.

■ AUTHOR INFORMATION

Corresponding Author

ywzhang@pku.edu.cn; yan@pku.edu.cn

Author Contributions

[†]These authors contributed equally.

Notes

The authors declare no competing financial interest.

■ ACKNOWLEDGMENTS

This work was supported by the NSFC (Grant Nos. 21025101 and 21271011). Y.W.Z. particularly appreciates the financial aid of China National Funds for Distinguished Young Scientists form the NSFC. The coauthors also thank Mr. Tao Zheng and Yefu Wang for their helps in the electron microscopic characterizations. We highly appreciate the constructive suggestions from the reviewers on this work.

■ REFERENCES

(1) (a) Somorjai, G. A. *Chem. Rev.* **1996**, *96*, 1223. (b) Ertl, G.; Knözinger, H.; Weitkamp, J. *Handbook of Heterogeneous Catalysis*; VCH: Weinheim, 1997. (c) Somorjai, G. A.; Li, Y. *Introduction to Surface Chemistry and Catalysis*, 2nd ed.; Wiley: Hoboken, N.J., 2010.

(2) Yang, X. M.; Skrabalak, S. E.; Li, Z. Y.; Xia, Y. N.; Wang, L. H. V. *Nano Lett.* **2007**, *7*, 3798.

(3) Taton, T. A.; Mirkin, C. A.; Letsinger, R. L. *Science* **2000**, *289*, 1757.

(4) Maier, S. A.; Brongersma, M. L.; Kik, P. G.; Meltzer, S.; Requicha, A. A. G.; Atwater, H. A. *Adv. Mater.* **2001**, *13*, 1501.

(5) Nilsson, A.; Pettersson, L. G. M.; Norskov, J. *Chemical Bonding at Surface and Interfaces*, 1st ed.; Elsevier: New York, 2008.

(6) (a) Tao, A. R.; Habas, S.; Yang, P. D. *Small* **2008**, *4*, 310. (b) Xia, Y.; Xiong, Y. J.; Lim, B.; Skrabalak, S. E. *Angew. Chem., Int. Ed.* **2009**, *48*, 60.

(7) (a) Jana, N. R.; Gearheart, L.; Murphy, C. J. *J. Phys. Chem. B* **2001**, *105*, 4065. (b) Jana, N. R.; Gearheart, L.; Murphy, C. J. *Adv. Mater.* **2001**, *13*, 1389. (c) Nikoobakht, B.; El-Sayed, M. A. *Chem. Mater.* **2003**, *15*, 1957. (d) Tsung, C. K.; Kou, X. S.; Shi, Q. H.; Zhang, J. P.; Yeung, M. H.; Wang, J. F.; Stucky, G. D. *J. Am. Chem. Soc.* **2006**, *128*, 5352. (e) Ye, X. C.; Jin, L. H.; Caglayan, H.; Chen, J.; Xing, G. Z.; Zheng, C.; Doan-Nguyen, V.; Kang, Y. J.; Engeta, N.; Kagan, C. R.; Murray, C. B. *ACS Nano* **2012**, *6*, 2804.

(8) (a) Okuno, Y.; Nishioka, K.; Kiya, A.; Nakashima, N.; Ishibashi, A.; Niidome, Y. *Nanoscale* **2010**, *2*, 1489. (b) Qu, Y. Q.; Cheng, R.; Su, Q.; Duan, X. F. *J. Am. Chem. Soc.* **2011**, *133*, 16730. (c) Ma, Y. Y.; Qu, Y. Q. *Nanoscale* **2012**, *4*, 3036.

(9) Zhang, H.; Xia, X. H.; Li, W. Y.; Zeng, J.; Dai, Y. Q.; Yang, D. R.; Xia, Y. N. *Angew. Chem., Int. Ed.* **2010**, *49*, 5296.

(10) (a) Joo, S. H.; Park, J. Y.; Renzas, J. R.; Butcher, D. R.; Huang, W. Y.; Somorjai, G. A. *Nano Lett.* **2010**, *10*, 2709. (b) Dagle, R. A.; Wang, Y.; Xia, G. G.; Strohm, J. J.; Holladay, J.; Palo, D. R. *Appl. Catal., A* **2007**, *326*, 213. (c) Urasaki, K.; Endo, K.; Takahiro, T.; Kikuchi, R.; Kojima, T.; Satokawa, S. *Top. Catal.* **2010**, *53*, 707. (d) Chen, A. H.; Miyao, T.; Higashiyama, K.; Yamashita, H.; Watanabe, M. *Angew. Chem., Int. Ed.* **2010**, *49*, 9895. (e) Abe, T.; Tanizawa, M.; Watanabe, K.; Taguchi, A. *Energy Environ. Sci.* **2009**, *2*, 315.

(11) (a) Nakao, Y.; Kaeriyama, K. *J. Colloid Interface Sci.* **1986**, *110*, 82. (b) Pan, C.; Pelzer, K.; Philippot, K.; Chaudret, B.; Dassenoy, F.; Lecante, P.; Casanove, M. -J. *J. Am. Chem. Soc.* **2001**, *123*, 7584. (c) Yan, X.; Liu, H.; Liew, K. Y. *J. Mater. Chem.* **2001**, *11*, 3387. (d) Viau, G.; Brayner, R.; Poul, L.; Chakroune, N.; Lacaze, E.; Fievet-Vincent, F.; Fievet, F. *Chem. Mater.* **2003**, *15*, 486. (e) Yang, J.; Lee, J. Y.; Deivaraj, T. C.; Too, H. -P. *J. Colloid Interface Sci.* **2004**, *271*, 308. (f) Tsukatani, T.; Fujihara, H. *Langmuir* **2005**, *21*, 12093. (g) Chakroune, N.; Viau, G.; Ammar, S.; Poul, L.; Veautier, D.; Chehimi, M. M.; Mangeney, C.; Villain, F.; Fiévet, F. *Langmuir* **2005**, *21*, 6788. (h) Harpeness, R.; Peng, Z.; Liu, X.; Pol, V. G.; Koltypin, Y.; Gedanken, A. *J. Colloid Interface Sci.* **2005**, *287*, 678. (i) Chen, Y.; Liew, K. Y.; Li, J. *Mater. Lett.* **2007**, *62*, 1018. (j) Zhang, Y. Q.; Yu, J. L.; Niu, H. J.; Liu, H. F. *J. Colloid Interface Sci.* **2007**, *313*, 503. (k) Brink, M. V.; Peck, M. A.; More, K. L.; Hoefelmeyer, J. D. *J. Phys. Chem. C* **2008**, *112*, 12122. (l) Lignier, P.; Bellabarba, R.; Tooze, R. P.; Su, Z. X.; Landon, P.; Ménard, H.; Zhou, W. Z. *Cryst. Growth Des.* **2012**, *12*, 939.

(12) (a) Yin, A. X.; Min, X. Q.; Zhang, Y. W.; Yan, C. H. *J. Am. Chem. Soc.* **2011**, *133*, 3816. (b) Yin, A. X.; Min, X. Q.; Zhu, W.; Wu, H. S.; Zhang, Y. W.; Yan, C. H. *Chem. Commun.* **2012**, *48*, 543. (c) Yin, A. X.; Min, X. Q.; Zhu, W.; Liu, W. C.; Zhang, Y. W.; Yan, C. H. *Chem.—Eur. J.* **2012**, *18*, 777.

(13) (a) Yin, Y. D.; Alivisatos, A. P. *Nature* **2005**, *437*, 664. (b) LaMer, V. K.; Dinegar, R. H. *J. Am. Chem. Soc.* **1950**, *72*, 4847.

(14) (a) Lele, S.; Anantharaman, T. R.; Johnson, CH. A. *Phys. Status Solidi* **1967**, *20*, 59. (b) Hinata, S.; Yanagisawa, R.; Saito, S.; Takahashi, M. *J. Appl. Phys.* **2009**, *105*, 07B718.

(15) (a) Witschy, J. K.; Beattie, J. K. *Inorg. Nucl. Chem. Lett.* **1969**, *5*, 969. (b) Kaziro, R.; Hambley, T. W.; Binstead, R. A.; Beattie, J. K. *Inorg. Chim. Acta* **1989**, *164*, 85.

(16) (a) Ataee-Esfahani, H.; Nemoto, Y.; Imura, M.; Yamauchi, Y. *Chem. Asian J.* **2012**, *7*, 876. (b) Hoshino, Y.; Eto, M.; Fujino, T.; Yukawa, Y.; Ohta, T.; Endo, A.; Shimizu, K.; Sato, G. P. *Inorg. Chim. Acta* **2004**, *357*, 600.

(17) (a) Puntes, V. F.; Zanchet, D.; Erdonmez, C. K.; Alivisatos, A. P. *J. Am. Chem. Soc.* **2002**, *124*, 12874. (b) Dumestre, F.; Chaudret, B.; Amiens, C.; Respaud, M.; Fejes, P.; Renaud, P.; Zurcher, P. *Angew. Chem., Int. Ed.* **2003**, *42*, 5213.

(18) Killin, D. S.; Prezhdo, O. V.; Xia, Y. N. *Chem. Phys. Lett.* **2008**, *458*, 113.

(19) Skriver, H. L.; Rosengaard, N. M. *Phys. Rev. B* **1992**, *46*, 7157.

(20) (a) Nakaya, U. *Snow Crystals: Nature and Artificial*; Harvard University Press: Cambridge, MA, 1954. (b) Magono, C.; Lee, C. W. *Journal of the Faculty of Science*; Series 7, Geophysics, Hokkaido University: Sapporo, Japan, 1966; Vol. 2, p 321. (c) Libbrecht, K. G. *Rep. Prog. Phys.* **2005**, *68*, 855. (d) Libbrecht, K. G. *Am. Sci.* **2007**, *95*, 52.

(21) (a) Libbrecht, K. G. *J. Cryst. Growth* **2003**, *258*, 168. (b) Gravner, J.; Griffeath, D. *Phys. Rev. E* **2009**, *79*, 011601.

(22) (a) Clark, L. W. *J. Am. Chem. Soc.* **1955**, *77*, 6191. (b) Haleem, M. A.; Yankwich, P. E. *J. Phys. Chem.* **1965**, *69*, 1729. (c) Boily, J. F.; Szanyi, J.; Felmy, A. R. *J. Phys. Chem. C* **2007**, *111*, 17072.

(23) (a) Ren, B.; Lin, X. F.; Yang, Z. L.; Liu, G. K.; Aroca, R. F.; Mao, B. W.; Tian, Z. Q. *J. Am. Chem. Soc.* **2003**, *125*, 9598. (b) Jiang, J.; Bosnick, K.; Maillard, M.; Brus, L. *J. Phys. Chem. B* **2003**, *107*, 9964. (c) Lu, Y.; Liu, G. L.; Lee, L. P. *Nano Lett.* **2005**, *5*, 5. (d) Yap, F. L.; Thoniyot, P.; Krishnan, S.; Krishnamoorthy, S. *ACS Nano* **2012**, *6*, 2056.

(24) (a) Cai, W. B.; Ren, B.; Li, X. Q.; She, C. X.; Liu, F. M.; Cai, X. W.; Tian, Z. Q. *Surf. Sci.* **1998**, *406*, 9. (b) Wang, Z. J.; Pan, S. L.; Krauss, T. D.; Du, H.; Rothberd, L. J. *Proc. Natl. Acad. Sci. U.S.A.* **2003**, *100*, 8638.

(25) (a) Schatz, G. C. *Acc. Chem. Res.* **1984**, *17*, 370. (b) Kneipp, K.; Kneipp, H.; Itzkan, I.; Dasari, R. R.; Feld, M. S. *Chem. Rev.* **1999**, *99*, 2957.
(26) Takenaka, S.; Shimizu, T.; Otsuka, K. *Int. J. Hydrogen Energy* **2004**, *29*, 1065.
(27) (a) Dagle, R. A.; Wang, Y.; Xia, G.; Strohm, J. J.; Holladay, J.; Palo, D. R. *Appl. Catal., A* **2007**, *326*, 213. (b) Kimura, M.; Miyao, T.; Komori, S.; Chen, A.; Higashiyama, K.; Yamashita, H.; Watanabe, M. *Appl. Catal., A* **2010**, *379*, 182.
(28) (a) Kelley, R. D.; Goodman, D. W. *Surf. Sci.* **1982**, *123*, L743. (b) Goodman, D. W. *Chem. Rev.* **1995**, *95*, 523.
(29) (a) Panagiotopoulou, P.; Kondarides, D. I.; Verykios, X. E. *Appl. Catal. A: Gen.* **2008**, *344*, 45. (b) Eckle, S. Investigations of the kinetics and mechanism of the selective methanation of CO in CO_2 and H_2-rich reformates over Ru supported catalysts. *Ph.D. Thesis*, Universitat Ulm, September 2012.